Longitudinal compression of a macrorelativistic electron beam

An Li, Jiaru Shi, Hao Zha,* Qiang Gao, Liuyuan Zhou, and Huaibi Chen
Department of Engineering Physics, Tsinghua University, Beijing 100084, People's Republic of China

(Received 15 June 2023; accepted 26 February 2024; published 8 April 2024)

We present a novel concept of longitudinal bunch train compression that can manipulate a relativistic electron beam across hundreds of meters. This concept holds the potential to compress the electron beam produced by a conditional linear accelerator at a high ratio, elevating its power to a level comparable with large induction accelerators. The method employs the spiral motion of electrons in a uniform magnetic field to fold hundreds-of-meters-long trajectories into a compact setup. The interval between bunches can be fine-tuned by modulating their spiral movement. We explore this method with the particle dynamic simulation. Compared to setups of similar size, such as a chicane, our method can compress bunches at considerably larger scales. Consequently, it opens up new possibilities for generating high-power beams using compact devices at lower costs.

DOI: 10.1103/PhysRevAccelBeams.27.044402

I. INTRODUCTION

Macropulses of high-power relativistic electrons have significant application potential across various research frontiers. They notably enhance acceleration gradients for the witness beam in the two-beam acceleration devices [1–4], potentially improve normal tissue protection in FLASH radiotherapy research [5], optimize imaging quality in FLASH radiography [6,7], and generate high flux, short neutron pulses in white neutron sources [8].

Nevertheless, the direct acceleration of a high-current electron beam to requisite energy poses significant technical and economic challenges. Conventional induction accelerators, typically spanning hundreds of meters, are employed in scientific setups for Z pinch or FLASH radiography [3,6,9], necessitating an extensive array of klystrons for power supply. Thus a more cost-efficient approach entails the acceleration of a long pulse beam at a suitable current, subsequently compressing it.

From the perspective of power compression methods, relativistic electron beams present numerous advantages as energy carriers, compared to alternatives like lasers [10,11], microwaves [12,13], and electric current [14,15]. These advantages include a high-energy conversion efficiency derived from ac power, and negligible energy dissipation during compression. Moreover, as the space charge effect diminishes with an increase in particle energy E, the power capacity of the electron beam is proportional to E^3. This suggests an extremely high-energy storage limit for the relativistic beam.

However, the compression of relativistic electron beams on nanosecond or microsecond scales poses a significant challenge due to the trajectory spanning hundreds of meters in spatial scale, which results in elevated costs and large setup dimensions. The Geel Electron LINear Accelerator Facility [8,16] and the Compact Linear Collider study [3,4] each performed macropulse compression tests at the nanosecond and microsecond scales, employing a permanent magnet of 50 tons and combiner rings with a diameter of up to 438 m, respectively. Hence, the typical electron beam compression is usually carried out at the level of picoseconds or femtoseconds [17–20].

In regard to this issue, we propose a novel method for compressing macrorelativistic electron beams. It offers the ability to manipulate beams on the scale of tens of nanoseconds, within a more compact system, thus providing an innovative solution for the cost-effective production of high-current relativistic electron beams.

II. COMPRESSING PRINCIPLE

As illustrated in Fig. 1, the spiral motion of electrons in a uniform magnetic field can be harnessed to fold hundreds of meters worth of trajectories into a compact cylindrical volume. This process allows for the efficient use of space, and we can manipulate bunches' interval by modulating the spiral helix of a bunch train.

To illustrate, let us consider the compression of two electron bunches depicted in Fig. 1. Assuming that the time interval between bunch 1 and bunch 2 is T_b at position I, and the cyclotron period of the bunch in the uniform magnetic field B_z is T_c. After modulation, bunch 1 gets a

*ZhaH@mail.tsinghua.edu.cn

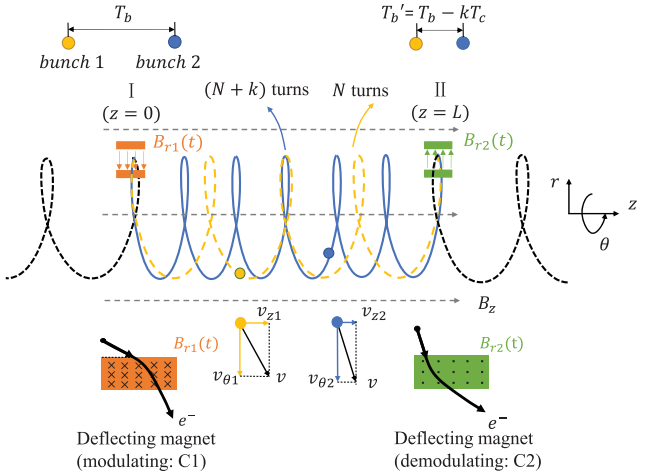

FIG. 1. Compressing principle. The electrons spiral forward in a uniform magnetic field B_z, and its velocity direction is deflected by two magnets at positions I and II. The deflecting magnets are dipole magnets with time-varying strength.

smaller spiral pitch (smaller velocity component in the z direction) than bunch 2. Their trajectories intersect again at position II after a drifting space. However, bunch 1 takes k extra spiral periods compared to bunch 2, and consequently, the interval between bunches at position II turns into $T_b' = T_b - kT_c$. A compression ratio $\eta = \frac{T_b}{|T_b - kT_c|}$ is achieved after the progress. The beam is compressed when $|\eta| > 1$. If $|\eta| < 1$, the beam is diluted.

Specifically, this modulation is achieved through the use of dipole magnets with time-varying strength. In Fig. 1, a pair of magnets is positioned along the particle trajectory to modulate and demodulate the bunch train velocities. The first magnet has a magnetic field oriented along $-\hat{r}$. It deflects the bunch, converting a portion of axial velocity v_z to angular component v_θ and reducing bunch's trajectory pitch. The time-varying strength of the dipole field leads to varying deflection effects on the bunch train, and each bunch spends different numbers of periods during the drift space of length L. At the focal point, another magnet with a field along $\hat{r}$ is placed, generating an opposite deflection effect. It sequentially restores the axial velocity components of each beam bunch, causing the compressed bunch train trajectory to align once again. For simplicity, in the following text, we will use the term "deflecting magnet" to refer to such electromagnetic dipole magnet.

Under the magnetic deflection modulation, it is important to note that the helical period of electrons with different v_z components remains consistent. The period, denoted as T_c, is solely determined by the electrons' relativistic mass and the uniform field intensity ($T_c = \frac{2\pi m}{eB_z}$).

The compressing method is similar to velocity bunching but tailored for relativistic electron beams. We cannot create a considerable velocity difference on a relativistic beam through energy modulation. However, the spiral motion allows us to expand the electrons' trajectories from one dimension to three dimensions. By modulating the axial component of the velocity, we achieve a "velocity bunching" method skillfully in relativistic situation.

This paper presents a detailed introduction to the compression methods, and we demonstrate its ability to manipulate the particle beam in two schemes, namely, bunch train compression and bunch train combination, with particle dynamic simulation.

Simulations of electromagnetic fields are performed with CST Studio Suite. For electron dynamics calculations, we utilized the tracking module in CST. Since this module is unable to handle beams with multipulse time structures, we developed MATLAB code to supplement such calculations. Our code exhibits good consistency with the dynamics calculations of single bunches obtained from CST in complex electromagnetic fields.

III. INSTALLATION AND COMPONENTS

As depicted in Figs. 2(a) and 2(b), the compression installation consists of several components: a large solenoid coil, injection/extraction structure, several deflecting magnets, and rf structures.

The main solenoid coil generates a uniform, axial-oriented magnetic field within its vacuum columnar cavity. The injection and extraction structures match the beam with the compression system. The deflecting magnets modulate the spiral motion of the bunch train, and the rf structures are employed for the longitudinal focusing of each bunch.

A. Solenoid

The solenoid coil has a length of 5 m, an outer diameter of 1 m, and an inner diameter of 0.8 m. The injection and extraction ports are separated by an axial distance of 3 m. The solenoid is divided into three sections, each of which

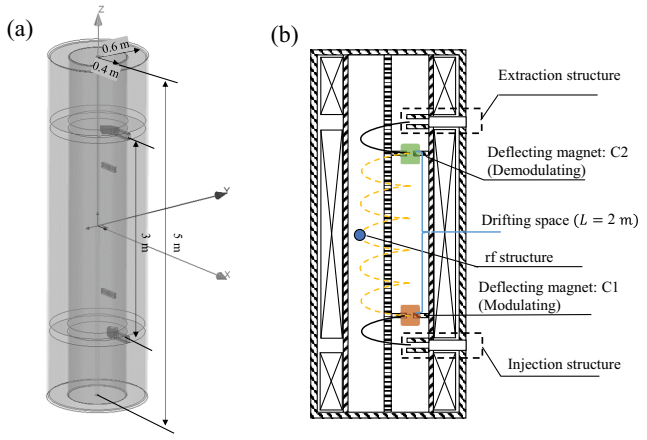

FIG. 2. (a) Compression installation and (b) the front view profile of the compression installation. It comprises a primary solenoid, injection, and extraction structures, several deflecting magnets, and rf Structures.

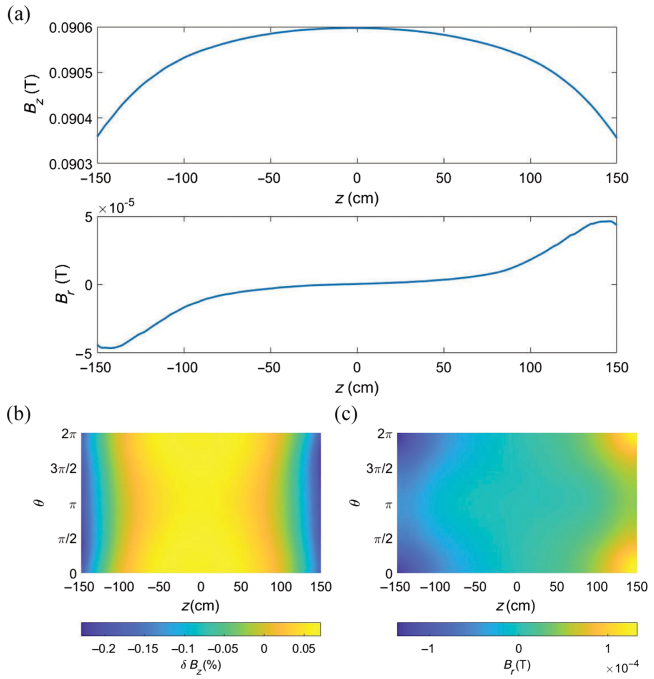

FIG. 3. Uniformity of magnetic field in the cavity. (a) Magnetic field component B_z and B_r along the z direction at $R = 25$ cm. (b) Uniformity of the axial magnetic field B_z on cylindrical surface $R = 25$ cm, where $\delta B_z = \frac{B_z - \overline{B_z}}{\overline{B_z}}$. (c) Distribution of radial magnetic field B_r. The field is obtained through a CST Studio simulation.

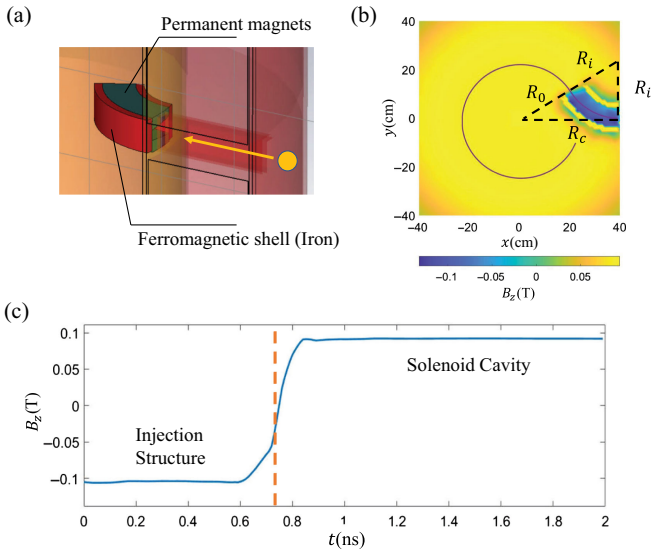

FIG. 4. (a) Injection structure. (b) Magnetic field B_z on injection plane and the simulated injected electron trajectory. (c) B_z observed on the injected electron's trajectory.

has an independently adjustable current, enabling precise control of the magnetic field distribution within the cylindrical cavity.

The simulated average magnetic field strength within the cavity is approximately 0.09 T. As an electron beam of 6.5 MeV is employed in the simulation, the reference spiral radius is 25 cm. The uniformity of the magnetic field on the cylindrical surface of $R_0 = 25$ cm is shown in Fig. 3. The axial magnetic field B_z has a maximum nonuniformity of less than 0.3%, and the radial component B_r is below 10^{-4} T.

B. Injection and extraction structures

The purpose of the injection structure is to induce spiral motion of the electron beam along the axis of the cylindrical cavity after injection. It is composed of ferromagnetic shells and permanent magnets with reversed magnetization to the uniform field [Fig. 4(a)].

The projection of the trajectory of the injected electrons consists of two arcs, as shown in Fig. 4(b). R_i and R_0 represent the radii of the electron's circular motion at the injection port and within the cavity, respectively, while R_c is the radius of the cylindrical cavity. With $R_0 = 25$ cm, $R_c = 40$ cm, and the geometric relationship, we can calculate that $R_i = 19.5$ cm, which corresponds to a magnetic field of $B_i = -0.11$ T for electrons with an energy of 6.5 MeV.

The simulated magnetic field distribution observed along the path of the injected electrons is shown in Fig. 4(c).

The extraction structure is symmetrically opposite to the injection structure to facilitate the extraction of spiral bunches from the solenoid.

C. Deflecting magnets

The deflecting magnets play a crucial role in modifying the axial velocity (v_z) of the incoming beam using their radial-oriented dipole magnetic field (B_r).

It should be noted that the deflecting magnets consist of yoke-less coils to avoid distortion in the uniform axial field and the beam's stable spiral movement. Consequently, the deflecting magnets exhibit significant fringe fields compared to an ideal sharp boundary magnetic field. Refer to Fig. 5(a) for the B_r distribution of the magnet on the cylindrical surface with $R_0 = 25$ cm.

In Fig. 5(b), the calculation for the deflecting effect of the nonuniformly distributed dipole field is demonstrated. To clarify, the axial velocity component (v_z) of the spiral electron is significantly smaller than the azimuthal velocity component (v_θ). Consequently, before and after the deflection, $z_{\text{out}} - z_{\text{in}} \ll R_0(\theta_{\text{out}} - \theta_{\text{in}})$.

By considering a narrow slice of width $Rd\theta$ at $\theta = \theta_0$, where the magnetic flux can be approximated as uniform $[B_r(z,\theta) = B_r(z,\theta_0)]$. The deflecting effect of the slice can be calculated as $dv_z(z) = \frac{e}{m} B_r(z,\theta_0) R_0 \cdot d\theta$, where e and m denote the charge and mass of the deflected relativistic electron, respectively. By integrating the deflection effect of each slice within a width of w, the overall deflection effect of the nonuniform field on the electrons can be obtained as $\Delta v_z(z) = \int \frac{e}{m} B_r(z,\theta) R_0 \cdot d\theta$.

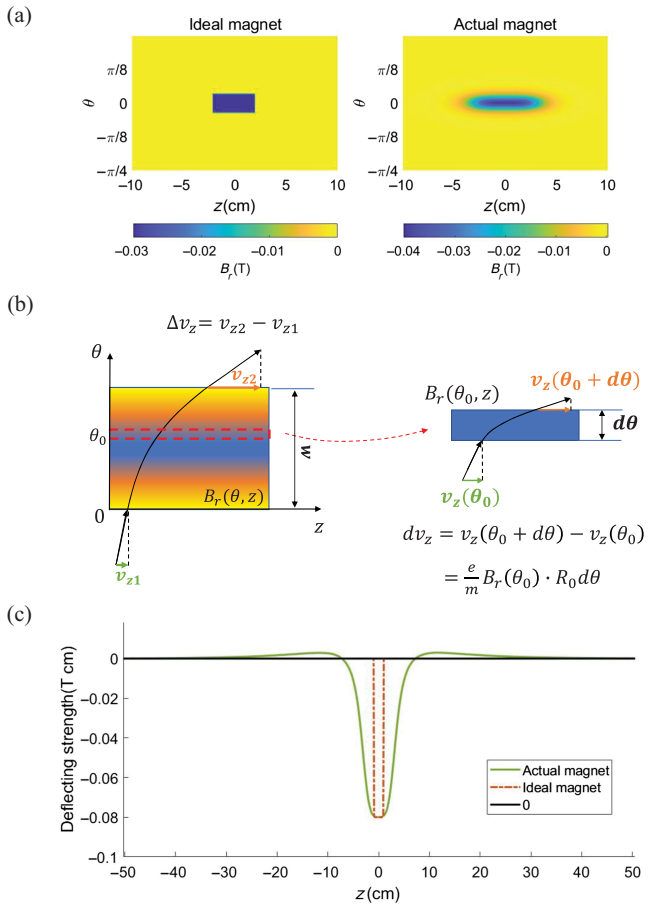

FIG. 5. (a) Magnetic field of ideal and actual deflecting magnets on the cylindrical surface of $R_0 = 25$ cm. (b) Deflecting strength Δv of the nonuniform magnetic field. (c) Integral field $\int B_r(\theta, z)R_0 \cdot d\theta$ of ideal and actual deflecting magnets. The field is obtained with CST simulation.

Figure 5(c) provides a visual representation of the distribution of the integral field $\int B(z, \theta)R_0 \cdot d\theta$ of the deflecting magnet along the z direction. Compared with the ideal magnet, the actual magnet exhibits a significantly wider range of magnetic field distribution. The fringe field of the magnet extends along the axial direction (z direction) for nearly 60 cm, which greatly exceeds the intended width of the designed good field region of only 2 cm.

The presence of the fringe field poses significant challenges to our magnet and system design. Electrons located outside the magnet are still influenced by the magnet's deflection. In Sec. IV, we will provide a detailed explanation on how to address the fringe field issue.

D. rf structure

As the turning period T_c is proportional to the electron's energy, dispersion of the beam can cause the longitudinal size of the bunches to grow, resulting in a deviation of the electrons' arrival time on the demodulating magnet.

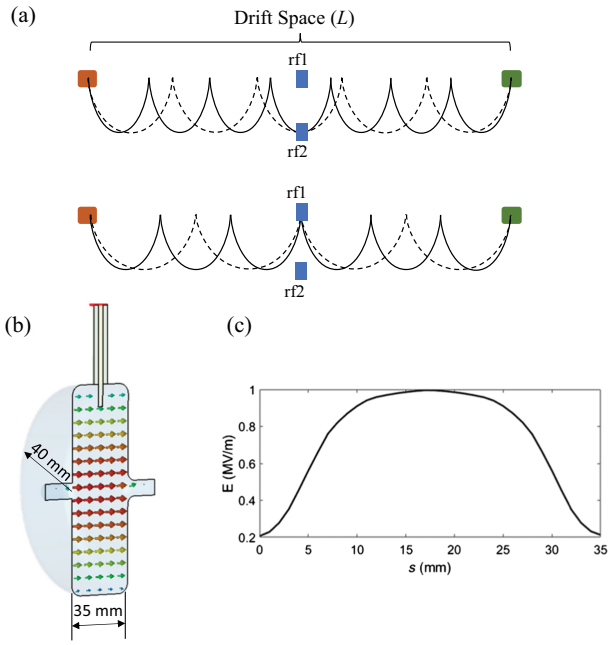

FIG. 6. (a) Position of the rf structures. (b) Cross section and electric field distribution of the rf cavity. (c) Accelerating gradient along the axis.

This time difference can cause incorrect demodulation of the electron's axial velocity and lead to particle loss.

Since the trajectory of each bunch is different, it is difficult to find suitable positions to place components for control and focusing. After comparing a series of options, we finally chose to place two rf structures in the middle of the drift space for focusing purpose, as shown in Fig. 6(a). Trajectories of bunches with even N intersect at the rf1 field, while the odd N trajectories intersect at the rf2 field. The rf fields can provide a certain degree of longitudinal focusing on each bunch. However, due to the difference in drift time, the focusing effect on each bunch is not the same. In our design, the voltage of rf fields are chosen to minimize the average size of extracted bunches.

The structure can be a pair of rf electrodes or an rf cavity, depending on the required rf field magnitude. For example, the cross section of a 3 GHz rf cavity used in our simulation is presented in Fig. 6(b). With an axial length of 35 mm, a radius of 40 mm, and an acceleration gradient amplitude of approximately 1 MV/m, The required rf peak power is 170 W. The accelerating gradient along the axis can be seen in Fig. 6(c).

IV. COMPRESSING METHODS

Based on the aforementioned installation, we demonstrate beam compression with several different ratio $\eta = \frac{T_b}{T_b'}$ [Fig. 7(a)].

Two distinct compression modes, bunch train compression ($T_b' \neq 0$) and bunch train combination ($T_b' = 0$) are

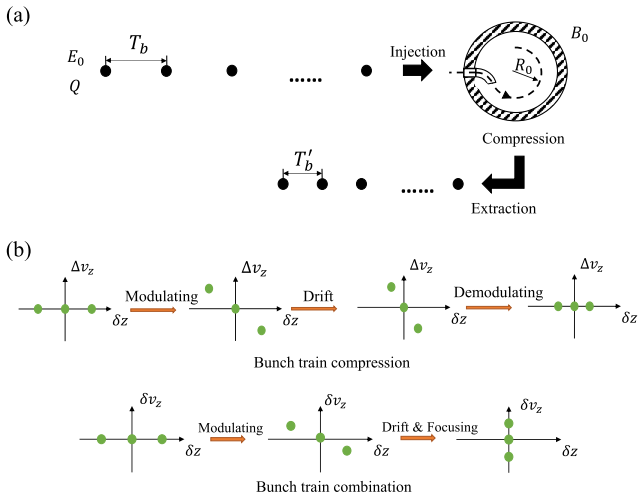

FIG. 7. (a) Sketch of bunch train compression. E_0 is the energy of the electrons, and Q denotes the charge of each bunch. (b) Compression process presented by phase space distribution of the bunch train in z direction.

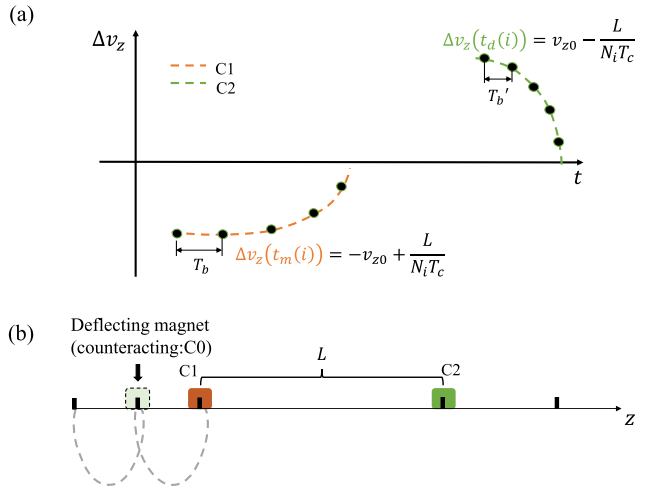

FIG. 8. (a) Time-varying deflecting effect of magnets in ideal situation. $t_m(i)$ and $t_d(i)$ denote the arrival times of the ith bunch at magnets C1 and C2. (b) Sketch of the relative position of the magnets.

discussed separately. The difference between the two methods can be simplified by explaining it in a two-dimensional phase space in the z direction as Fig. 7(b).

A. Bunch train compression

1. Discussion about deflecting magnets

In the ideal situation, all beam bunches have an initial axial velocity v_{z0} after injection. As the ith bunch should has a uniform pitch of $P_i = \frac{L}{N_i}$ in the drift region, the deflecting magnet C1 should deflect it by $\Delta v_i = -v_{z0} + \frac{L}{N_i T_c}$. We can easily calculate the time-dependent strength of the magnet [Fig. 8(a)]. Similarly, the magnet C2 for demodulation should deflect the bunches by $\Delta v_i' = v_{z0} - \frac{L}{N_i T_c}$ at the end of the drift region.

However, the fringe field of time-varying magnets greatly complicates the problem. Before modulation, the injected beam may deviate from the magnet's good field region. After modulation, bunches' trajectory pitch may be nonuniform in drift space. Setting the deflecting magnet strength according to Fig. 8(a) would lead to severe particle loss.

To address this issue, another deflecting magnet C0 was added between the injection port and the modulating magnet, as shown in Fig. 8(b), to counteract the effect of the modulating magnet's fringe field on the injection side. What is more, an iterative calculation method was employed to obtain the time-varying currents of the three magnets. The objective of the calculation was to ensure that each bunch (i) reaches the center of the modulating magnet's good field region after injection, (ii) reaches the center of the demodulating magnet's good field region after drifting, and (iii) finally exits the solenoid installation through the extraction port. After determining the geometry of the magnets and the parameters of the bunch train, we can solve for the required time-varying strength of each magnet.

2. Simulation

Our simulation employed a solenoid cavity with a uniform magnetic field strength of $B_z = 0.09$ T and electron beam with an average energy of $E_0 = 6.5$ MeV. Each bunch has a charge of $Q = 1$ nC. The cyclotron radius of the electrons in the uniform magnetic field is $R_0 = 25$ cm and the period is $T_c = 5.4$ ns.

The phase-space acceptance of this compression system is shown in Fig. 9. In the spiral motion, the vertical (y) and horizontal (x) directions of the phase space coordinate system align closely with the z and r directions of the laboratory cylindrical coordinate system, respectively. The geometric acceptance in the two directions is 15 and 780 mm mrad. The aperture of this system is quite large. The energy acceptance range of the system for a 6.5 MeV beam is approximately $\pm 5‰$. If each bunch with dispersion $|\delta| < 5‰$ is injected with a pulse width of less than 0.2 ns, particle losses caused by deflection errors during the modulating and the demodulating process can be completely avoided, thus achieving 100% compression efficiency.

The phase-space transformation of a single bunch before and after the compression in vertical and longitudinal directions is shown in Fig. 10. The magnet's fringe field introduces nonlinearity in this transmission system, causing some distortion to bunch's transverse ellipse envelope.

With the T_c determined, the compression ratio η depends on the initial interval T_b between the beam bunches. We will present the simulation results for two compression ratios $\eta_1 = 5$ and $\eta_2 = 10$.

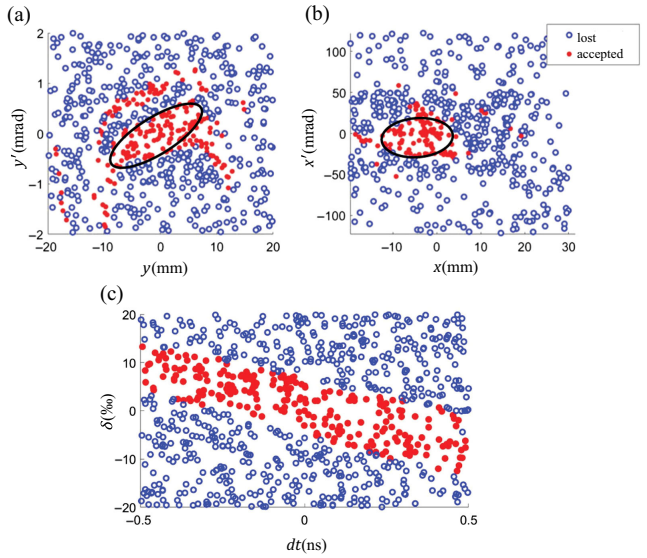

FIG. 9. Phase-space acceptance of the compression system in (a) vertical, (b) horizontal, and (c) longitudinal directions. $\delta = \delta E/E_0$. "Accepted" denotes the particle can be captured by the compressed beam, and "lost" is the converse.

In the two cases, we employ a beam consisting of 10 bunches with an initial interval of $T_{b1} = 6.8$ ns and $T_{b2} = 6$ ns, corresponding to a beam length of approximately 68 and 60 ns. The amplitude of the rf fields (Fig. 6) used for longitudinal focusing is 28 and 25 kV, respectively, and the frequency is $f_1 = f_2 = 3$ GHz.

During the compression process, the first bunch undergoes 17 spiral periods from injection to the extraction port, the second bunch takes 16, and so on.

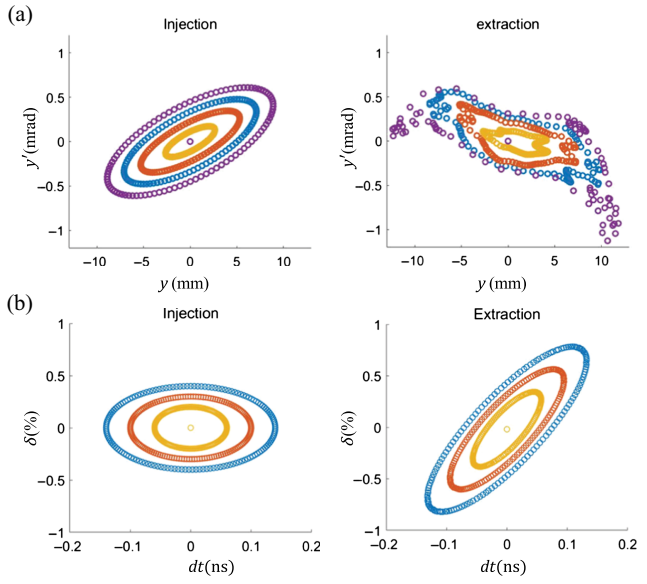

FIG. 10. Phase-space distribution transformation of the first injected bunch before and after the compression in (a) z direction and (b) longitudinal direction.

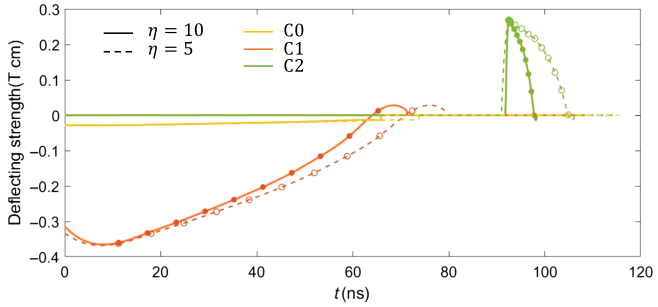

FIG. 11. Calculated time-varying strength of the deflecting magnets. The solid and dashed lines denote situations with compression ratio $\eta = 10$ and $\eta = 5$, respectively. The dots denote the arrival time of bunches at magnets C1 and C2.

The time-varying strengths of the deflecting magnets obtained through iterative calculation are shown in Fig. 11. The peak power required for the deflection magnet is 2.2 kW, with a maximum frequency of 40 MHz.

In the simulation, the profile of each bunch before the injection is shown in Fig. 12(a). The bunch has an initial rms length of 0.1 ns and maximum energy spread of $\delta = \pm 5‰$. The initial emittance of the beam is 1 mm mrad in both r and z directions.

For $\eta = 5$ and $\eta = 10$, current profile of the beam before and after the compression are shown in Figs. 12(b) and 12(c), respectively. The full width at half maximum of the compressed bunches are different because the

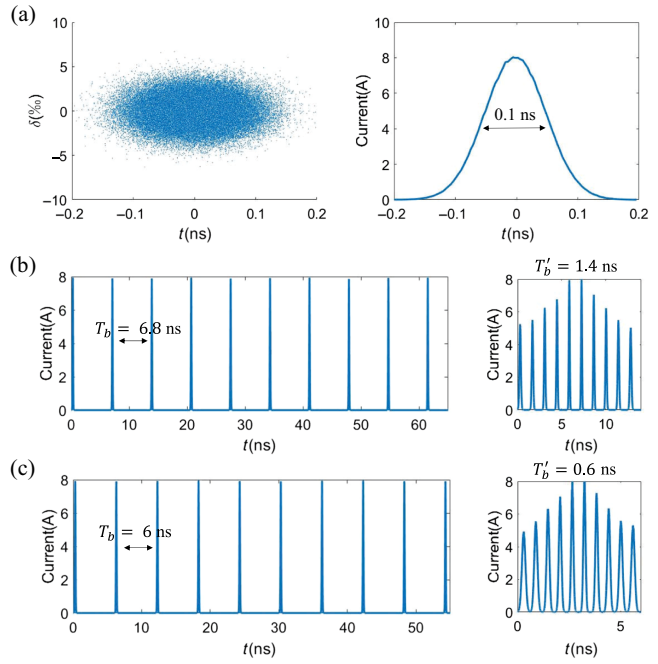

FIG. 12. (a) Profile of each injected bunch. (b) Current profile of the beam before (left) and after (right) the compression with $\eta = 5$. (c) Current profile of the beam before (left) and after (right) the compression with $\eta = 10$.

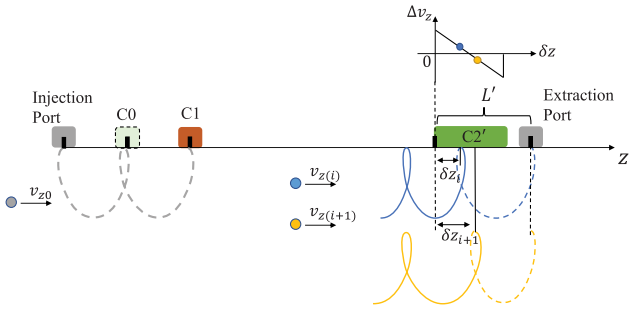

FIG. 13. Sketch of the bunch train combination system.

amplitude of the focusing rf field is constant, but the drift time of each bunch is inconsistent.

In the case of $\eta = 10$, the interval between the bunches is reduced from $T_b = 6$ ns to $T_b' = T_b - T_c = 0.6$ ns, resulting in a compression with a ratio of 10. The average current of the beam string increased from 0.17 to 1.7 A, and the average power increased from 1.1 to 11 MW.

We have identified several limiting factors for further improving the compression ratio. The magnet's fringe field limits the minimum pitch of the electron spiral trajectory, which restricts the maximum number of bunches in the bunch train. Moreover, the time-varying voltage of the demodulating magnet C2 limits the minimum spacing between the extracted bunches, particularly when a magnet without a yoke is used. If T_b' is further reduced, a faster change in demodulating strength is required.

However, there is a limiting case, $T_b' = 0$, which can be achieved by employing another demodulation method.

B. Bunch train combination

1. Discussion about deflecting magnets

If the injected bunch interval T_b is equal to cyclotron period T_c, all the bunches will arrive at the demodulating magnet C2 simultaneously after the spiral procedure. In this case, the time-varying magnet described in the previous section cannot demodulate the axial velocity of the bunch train.

We can employ a spatial-gradient magnet instead of the time-varying magnet for demodulation and focus all the bunches at the extraction port.

The bunch train combination system is illustrated in Fig. 13. The configuration of magnets C0 and C1 is the same as in the previous section. The ideal deflecting strength of demodulating magnet C2 is linearly related to the coordinate δz. The demodulation progress for the ith bunch in the axial direction satisfies the following equation:

$$[v_{z(i)} + \Delta v_z(\delta z_i)] \cdot T_c = L' - \delta z_i.$$

From a phase-space perspective, as shown in Fig. 7(b), we rotate the bunch train that was originally distributed along the z axis to the δv_z axis after the spiral procedure.

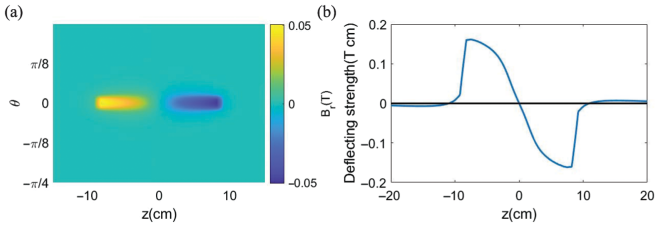

FIG. 14. (a) Radial magnetic flux and (b) deflecting strength distribution of demodulating magnets.

At the extraction port, from the spatial perspective, bunches overlap with each other and seem like a large bunch.

The simulated magnetic flux density of the designed spatial-gradient magnet on a cylindrical surface $R_0 = 25$ cm is depicted in Fig. 14(a), and its deflecting strength along the z direction is shown in Fig. 14(b). The linear relationship holds within a good field region spanning approximately 6 cm.

By iteratively solving for the time-varying strengths of C0 and C1, along with the demodulating coordinates δz_i for each bunch, the magnet parameters suitable for the bunch train combination can be obtained, taking into account the presence of fringe fields.

2. Simulation

In the simulation of bunch train combination, parameters of bunches, solenoid field, injection, and extraction port are consistent with the compression mode.

The transverse phase-space acceptance of the combination system is shown in Fig. 15(a). The geometric acceptance in vertical and horizontal directions are 1.2 and 2.5 mm mrad. The longitudinal acceptance is consistent with the previous compression mode.

We simulated two scenarios: (i) combining a beam of 10 bunches, each with a charge of 1 nC, into a single large bunch and (ii) periodically merging every three adjacent 1 nC bunches into a cluster.

In the first scenario, the time-varying deflecting strength of magnets C0 and C1 is shown in Fig. 16(a). The current profile of the beam before and after combinations is

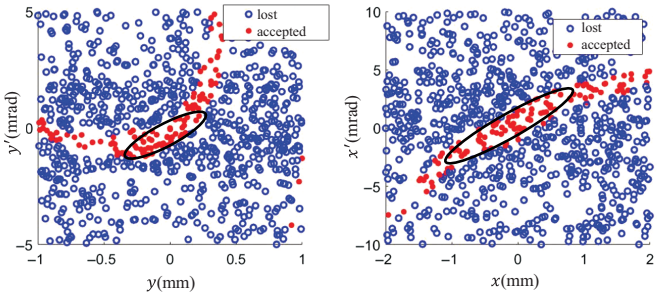

FIG. 15. Transverse acceptance of the combination system. Accepted denotes the particle can be captured by the compressed beam, and lost is the converse.

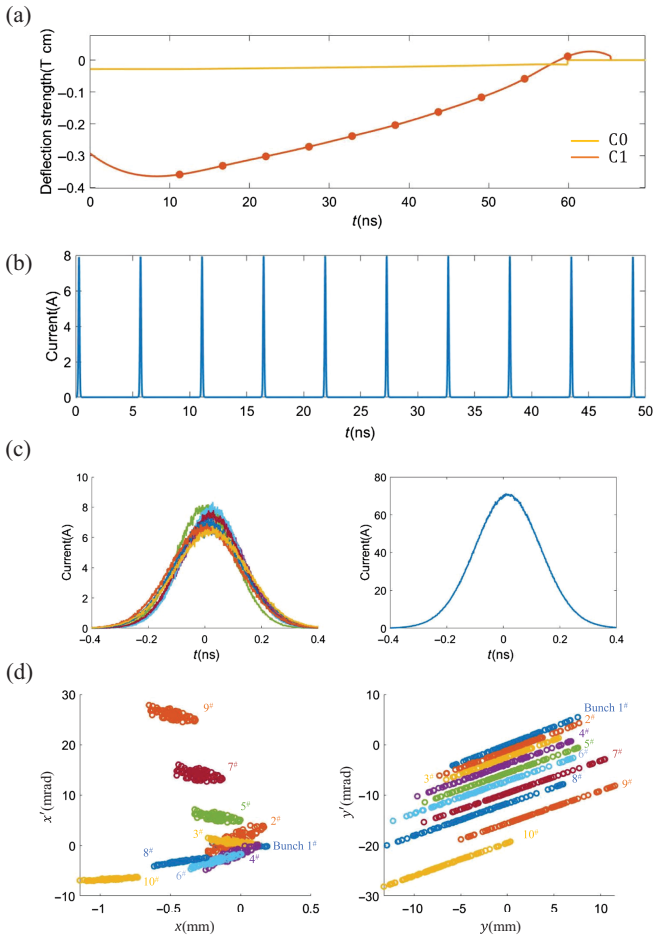

FIG. 16. (a) Time-varying deflecting strength of magnets. (b) Current profile of injected beam. (c) Current profile of individual bunches (left) and the combined bunch (right) at extraction port. (d) Transverse phase-space distribution of the combined bunch.

depicted in Figs. 16(b) and 16(c). Charge of the combined bunch is 10 nC, and peak current of the beam is multiplied by a factor approximately of 9. Figure 16(d) illustrates the transverse phase-space distribution of the combined bunch, confirming its alignment with expectations as bunches are stacked along the vertical direction.

In the second scenario, the intensity of the deflecting magnet C1 varies over time in a periodic manner [Fig. 17(a)]. After passing through the device, every three adjacent bunches merge into one. The average current of the beam remains unchanged, while the peak current is approximately 3 times higher than the injection.

Though this combination method produces bunch with a large charge, the emittance is also large. If the bunch keeps on drifting for a period of time without postfocusing, it will spread out again. Therefore, this method may not be suitable for applications that are strict on electron beam emittance, while it is appropriate for applications such as white spectrum neutron sources [8], where the combined

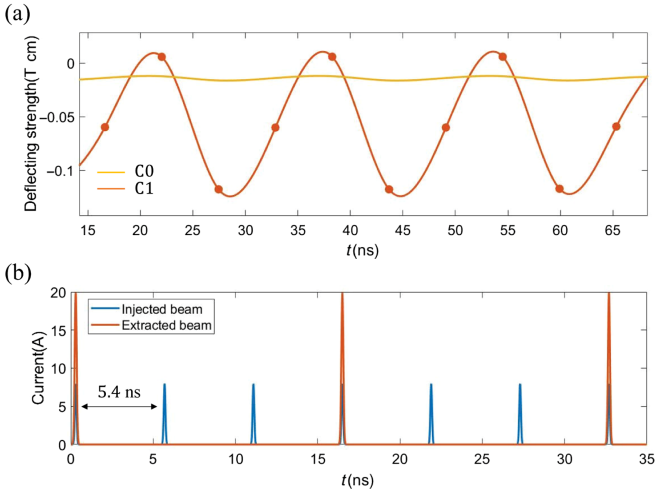

FIG. 17. (a) Time-varying deflecting strength of magnets. (b) Current profile of Injected and extracted beam.

bunch hits the target after combination and the emittance of the bunch is insignificant.

V. SUMMARY AND OUTLOOK

In this paper, we demonstrate a macroelectron beam compression concept achieved by modulating bunches' spiral motion in a uniform magnetic field. With the proposed system, a simulation of two different compressing schemes is performed.

This method is capable of compressing electron beams on a scale of tens of nanoseconds using a relatively compact device (<10 m in spatial scale). It offers high compression efficiency and large energy storage limits, making it a promising choice for power compression.

There are several aspects of our research that can be further improved. For instance, support and power feeding structures of the rf cavity remain unaddressed. We prioritized a holistic analysis of the transportation system over individual component scrutiny due to the diversity of the bunch trajectory and issues with component fringe fields. In addition, the impact of synchrotron radiation effects may pose a limitation on our objective to augment the energy of compressed electrons. This concept has to be further refined using tools and methods of modern accelerator physics.

[1] C. Jing, S. Antipov, M. Conde, W. Gai, G. Ha, W. Liu, N. Neveu, J. Power, J. Qiu, J. Shi, D. Wang, and E. Wisniewski, Nucl. Instrum. Methods Phys. Res., Sect. A **898**, 72 (2018).

[2] J. Shao, C. Jing, S. Antipov, M. Conde, W. Gai, Q. Gao, and G. Ha, in *Proceedings of the 8th International Particle Accelerator Conference, IPAC-2017, Copenhagen, Denmark*, (JACoW, Geneva, Switzerland, 2017), pp. 3305–3307.

[3] A multi-TeV linear collider based on CLIC technology: CLIC Conceptual Design Report, edited by M. Aicheler, P. Burrows, M. Draper, T. Garvey, P. Lebrun, K. Peach, N. Phinney, H. Schmickler, D. Schulte, and N. Toge, CERN-2012-007, 2012.

[4] F. Tecker, R. Corsini, L. Rinolfi, C. Biscari, A. Ghigo, M. Preger, P. Royer, and A. Ferrari, in *Proceedings of the 20th Particle Accelerator Conference, PAC-2003, Portland, OR* (IEEE, New York, 2003), pp. 684–686.

[5] J.-L. Ruan, C. Lee, S. Wouters, I. D. Tullis, M. Verslegers, M. Mysara, C. K. Then, S. C. Smart, M. A. Hill, R. J. Muschel *et al.*, Int. J. Radiat. Oncol. Biol. Phys., Suppl. **111**, 1250 (2021).

[6] M. Burns, B. Carlsten, T. Kwan, D. Moir, D. Prono, S. Watson, E. Burgess, H. Rutkowski, G. Caporaso, Y.-J. Chen, S. Sampayan, and G. Westenskow, in *Proceedings of the 1999 Particle Accelerator Conference, New York, 1999* (IEEE, New York, 1999), pp. 617–621.

[7] B. Cassany, B. Cadilhon, P. Modin, and R. Pecquois, in *Proceedings of the 2013 Abstracts IEEE International Conference on Plasma Science, ICOPS, San Francisco, CA* (IEEE, Piscataway, NJ, 2013), p. 1.

[8] A. Bensussan and J. Salome, Nucl. Instrum. Methods **155**, 11 (1978).

[9] M. G. Haines, S. V. Lebedev, J. P. Chittenden, F. N. Beg, S. N. Bland, and A. E. Dangor, Phys. Plasmas **7**, 1672 (2000).

[10] D. Strickland and G. Mourou, Opt. Commun. **56**, 219 (1985).

[11] J. M. Mikhailova, A. Buck, A. Borot, K. Schmid, C. Sears, G. D. Tsakiris, F. Krausz, and L. Veisz, Opt. Lett. **36**, 3145 (2011).

[12] T. Sugimura, T. Kamitani, K. Yokoyama, K. Kakihara, M. Ikeda, and S. Ohsawa, in *Proceedings of the 22nd International Linear Accelerator Conference, LINAC-2004, Lubeck, Germany* (CERN, Geneva, Switzerland, 2004), pp. 754–756.

[13] N. Catalan Lasheras, H. Damerau, R. Gerard, A. Grudiev, T. Lucas, G. McMonagle, J. Paszkiewicz, S. Pitman, A. Magazinik, i. Syratchev, A. Vnuchenko, M. Volpi, B. Volpi, W. Wuensch, and V. Romano, in *Proceedings of the 9th International Particle Accelerator Conference, IPAC-2018, Vancouver, BC, Canada* (CERN, Geneva, Switzerland, 2018), pp. 2545–2548.

[14] R. Cassel (2000), https://www.osti.gov/servlets/purl/784769.

[15] S. G. Tantawi, C. D. Nantista, V. A. Dolgashev, C. Pearson, J. Nelson, K. Jobe, J. Chan, K. Fant, J. Frisch, and D. Atkinson, Phys. Rev. ST Accel. Beams **8**, 042002 (2005).

[16] D. Tronc, J. Salomé, and K. Böckhoff, Nucl. Instrum. Methods Phys. Res., Sect. A **228**, 217 (1985).

[17] S. G. Anderson, P. Musumeci, J. B. Rosenzweig, W. J. Brown, R. J. England, M. Ferrario, J. S. Jacob, M. C. Thompson, G. Travish, A. M. Tremaine, and R. Yoder, Phys. Rev. ST Accel. Beams **8**, 014401 (2005).

[18] B. E. Carlsten and S. J. Russell, Phys. Rev. E **53**, R2072 (1996).

[19] S. Vartak and N. Lawandy, Opt. Commun. **120**, 184 (1995).

[20] C. Lu, T. Jiang, S. Liu, R. Wang, L. Zhao, P. Zhu, D. Xiang, and J. Zhang, Phys. Rev. Lett. **120**, 044801 (2018).